NUCLEIC ACID THERAPEUTICS
Volume 34, Number 1, 2024
Mary Ann Liebert, Inc.
DOI: 10.1089/nat.2023.0018

Open camera or QR reader and scan code to access this article and other resources online.

Biodistribution of Radioactively Labeled Splice Modulating Antisense Oligonucleotides After Intracerebroventricular and Intrathecal Injection in Mice

Tom Metz,[1] Mick M. Welling,[2] Ernst Suidgeest,[3] Esmée Nieuwenhuize,[1] Thomas de Vlaam,[4] Daniel Curtis,[4] Tsinatkeab T. Hailu,[4] Louise van der Weerd,[1,3,*] and Willeke M.C. van Roon-Mom[1,*]

Antisense oligonucleotides (AONs) are promising therapeutic candidates, especially for neurological diseases. Intracerebroventricular (ICV) injection is the predominant route of administration in mouse studies, while in clinical trials, intrathecal (IT) administration is mostly used. There is little knowledge on the differences in distribution of these injection methods within the same species over time. In this study, we compared the distribution of splice-switching AONs targeting exon 15 of amyloid precursor protein pre-mRNA injected via the ICV and IT route in mice. The AON was labeled with radioactive indium-111 and mice were imaged using single-photon emission computed tomography (SPECT) 0, 4, 24, 48, 72, and 96 h after injection. *In vivo* SPECT imaging showed ^{111}In-AON activity diffused throughout the central nervous system (CNS) in the first hours after injection. The ^{111}In-AON activity in the CNS persisted over the course of 4 days, while signal in the kidneys rapidly decreased. Postmortem counting in different organs and tissues showed very similar distribution of ^{111}In-AON activity throughout the body, while the signal in the different brain regions was higher with ICV injection. Overall, IT and ICV injection have very similar distribution patterns in the mouse, but ICV injection is much more effective in reaching the brain.

Keywords: antisense oligonucleotide, distribution, mouse brain, SPECT imaging, intrathecal administration, intracerebroventricular administration

Introduction

Splice-modulating antisense oligonucleotides (AONs) are promising drugs in central nervous system (CNS) diseases in preclinical as well as in clinical studies [1,2]. Systemically delivered AONs hardly reach the CNS due to the blood-brain barrier (BBB) [3]. The delivery of AONs to the CNS in patients is currently performed by direct injection into the cerebrospinal fluid (CSF) by means of intrathecal (IT) injection [4]. This delivery method bypasses the BBB by injection into the subarachnoid space of the spinal cord where AONs can pass the pia mater and enter the parenchyma. There is very limited human data available on how AONs spread through the different brain regions after IT injection. Clearance from the CNS is mainly determined by two factors, the rate of transfer to the CSF and ASO degradation [5]. Tissue half-life in CNS is chemistry dependent, but in preclinical studies, it ranges from 3 weeks to 6 months [6–8].

Data from deceased patients in clinical trials of a splice modulating AON for spinal muscular atrophy injected IT showed highest AON concentrations in caudal regions, such as lumbar and thoracic spinal cord, compared to rostral regions, such as cervical spinal cord and the brain [4,7,9]. A study in cynomolgus monkeys shows that the rostral distribution of IT-injected AON can be improved by increasing the volume of the dose [10].

In preclinical research, mice are often used as a first *in vivo* model to study the effects of AONs on CNS diseases. In

[1]Department of Human Genetics; [2]Interventional Molecular Imaging Laboratory, Department of Radiology; and [3]Department of Radiology; Leiden University Medical Center, Leiden, The Netherlands.
[4]Amylon Therapeutics, Leiden, The Netherlands.
*Shared last author.

contrast to AON administration in humans, intracerebroventricular (ICV) injection into the lateral ventricle of the brain is the main route of delivery used in these models. The CSF distributes compounds, such as AONs, in the brain via bulk flow, through the ventricular spaces, down the spinal cord, and through the glymphatic system [11].

A different site of injection can therefore greatly impact the final AON dose at the target region. However, there are no direct comparisons of IT and ICV administration routes, hampering the translation to humans. In preclinical experiments, there is only *in vivo* distribution data of IT-injected AONs in rats, but not for mice. A gapmer AON-injected IT in rats spreads to the cranium directly after injection, but penetration into deeper brain structures takes longer [12]. In CNS areas, such as cerebral cortex, hippocampus, and spinal cord, the effect of the AON was highest after 4 weeks, with less effect in deeper brain areas such as the striatum. In addition, the presence of AONs correlated well with protein suppression.

In the current study, we investigated the distribution of a splice modulating AON [22-mer fully modified with 2′-methoxy ethyl (2′-MOE) and a phosphorothioate (PS) backbone] over time, using two administration routes: ICV and IT. Distribution of splice modulating AONs has been revealed by measuring the exon skipping levels in different brain regions [2,13], but the distribution over the first 4 days after administration in live animals in the brain has not been studied. The AON was designed and tested *in vitro* and *in vivo* previously and targets the amyloid precursor protein (*APP*) pre-mRNA [2]. Our previous research has shown that AON treatment leads to exon skipping *in vitro* and injection of this AON in a mouse has shown an exon skipping effect in several brain areas [2].

Here, we analyze the biodistribution of this same AON with a radioactive label in the first hours and days after IT and ICV injection in mice using single-photon emission computed tomography (SPECT) imaging. The advantage of measuring the distribution with SPECT is that it can be performed repeatedly in the same animal over time and the signal can be measured throughout the whole body [14]. We show that, after AON injection, the tracer persists in the CNS, while rapidly declining from the rest of the body. As expected, injections in the lateral ventricle (ICV) gave a much higher signal in the CNS compared to IT injections in mice, but the distribution across the body and brain is similar.

Materials and Methods

Animals

For this study, male wild-type mice with a C57BL/6 (B6) and 129S background were used. All experiments were carried out in accordance with European Communities Council Directive 2010/63/EU and were approved by the Leiden University Animal Ethical Committee (AVD11600201 85405). Animals were group housed in individually ventilated cages in a 12 h light/dark cycle at 20°C–22°C with standard chow food and water available *ad libitum*. Cage enrichment consisted of bedding material, a wooden gnawing stick, and a cardboard roll. Female and male mice were 3.6 ± 0.2 months of age at the start of the experiment. During the 4 days of the experiment the mice were individually housed to avoid cross-contamination of excreted radioactive metabolites.

AON AON-DOTA design

The AON used in this study is a 22-mer fully modified with 2′-MOE and PS backbone modifications and binds on the junction of intron 14 and exon 15 of mouse APP pre-mRNA (ENSMUST00000005406.12, Table 1). The AON was designed according to guidelines previously published [15]. For the radioactive labeling of the AON, a 1,4,7,10-tetraazacyclododecane-1,4,7,10-tetraacetic acid (DOTA)-coupled AON (AON-DOTA) was purchased from Axolabs (Kulmbach, Germany). The DOTA moiety was covalently bound to the 3′ side of the AON with a linker (CATCTTCAGCAA AGAACACCTT-NH_2C_6-DOTA) [16]. Radioactive labeling was achieved with indium 111 with primary energies of 171.3 keV (91%) and 245.4 keV (94%), half-life 2.8049 days.

Cell transfection with AON and AON-DOTA

To test if the DOTA-coupled AON retained its exon skipping efficiency, transfection of AON-DOTA was compared to transfection with the AON without DOTA chelation in mouse neuroblastoma cells (N1E-115-1). Neuroblastoma cells were maintained on Dulbecco's modified Eagle's medium with high glucose (41966; Gibco) supplemented with 10% fetal bovine serum and 1% penicillin/streptomycin. Cells were seeded in a 12-well plate for 24 h and transfected with 12.5, 25, 50, and 100 nM AON or AON-DOTA using Lipofectamine 2000 (11668; Invitrogen) in OptiMEM serum-free medium (31985; Gibco) for 20 min. The medium was replaced with a serum-containing medium after 4 h. Cells were harvested for RNA isolation 72 h after transfection.

Synthesis of ^{111}In-labeled AON

To replace the Dulbecco's phosphate-buffered saline (DPBS) (Full name, 14190; Gibco) buffer, wherein the AON stock was dissolved with NH_4OAc buffer pH 7.0, the AON in DPBS was centrifuged in a size-exclusion filter column (Amicon 3K, 0.5 mL) three times at 14,000*g* for 30 min adding 0.5 mL NH_4OAc buffer after each step. The final volume was 100 μL at a concentration of $\sim$10 mg/mL. The AON solution was mixed with 300 μL $InCl_3$ (111 MBq; Curium Netherlands Holding BV, s Hertogenbosch, The Netherlands) and 600 μL NH_4OAc pH 6.5 buffer and incubated for 20 min at 60°C. To wash out the NH_4OAc buffer containing unbound ^{111}In, the labeled AON solution was purified using centrifugation in a filter column as described above using DPBS as the washing buffer.

Table 1. Antisense Oligonucleotide and Polymerase Chain Reaction Primer Sequences

Name	*Sequence*
Mouse APP exon 15 AON	CATCTTCAGCAAAGAACACCTT
Mouse APP exon 14 forward primer	TCTGGGCTGACAAACATCAA
Mouse APP exon 16 reverse primer	TTCTGCTGCATCTTGGAGAG

AON, antisense oligonucleotide; APP, amyloid precursor protein.

After the last washing step, the column was centrifuged upside down at 1,000*g* for 5 min to collect the radiolabeled AON. With counting radioactivity of the purified ^{111}In-labeled AON and the activity of the washing steps, yield was determined at 95.8% ± 0.3%. Using thin layer chromatography with water as mobile phase, the purity was assessed at 98.0% ± 2.0% [14].

Mouse injections

For IT injections, mice were anesthetized using 3.5% isoflurane (0.8 L/min) in medical air and maintained under anesthesia with 1.5% isoflurane (0.4 L/min). The back of the mouse was shaven and fixed with the thumb, index finger and middle finger on the spine with tips of fingers touching the hip bone [17]. Injection was performed using a Hamilton gastight 10 μL luer-lock syringe and a 30G disposable needle. Dead volume was avoided by priming the syringe and needle with AON solution. The needle was inserted in between L5 and L6 of the spine at an angle of 80° to the horizontal, bevel facing upwards and toward the tail of the mouse.

When the needle touched the bone of the spinal column, the needle was lowered to an angle of 30° to the horizontal. A tail-flick indicated correct insertion of the needle. The angle could be lowered until a tail flick was observed. The total volume of 10 μL labeled AON, with a total administered dose of 220 ± 21 μg AON per mouse (measured with spectrophotometer), was injected into the spinal canal at 1 μL/s.

The ICV injections were done as previously described [18]. In short, mice were anesthetized and analgesia was administered. Craniotomy into the right lateral ventricle with a total volume of 10 μL was performed at 1 μL/s. After injection, the cannula guide was either fixed to the skull or it was removed and the skin was sutured. Directly after injection and before the first SPECT scan, whole-body activity (MBq) of the mice was measured using a dose calibrator (VDC101; Veenstra Instruments, The Netherlands).

General SPECT imaging

To follow the localization of the injected tracers for 96 h, SPECT scanning was performed using a three-headed U-SPECT-II (MILabs, Utrecht, The Netherlands) as described previously [19]. Mice were anesthetized using 3.5% isoflurane (0.8 L/min) and maintained under anesthesia with 1.5% isoflurane (0.4 L/min) during each scan for 20 min. Total body scans were acquired using a 0.6 mm mouse pinhole collimator, and energy setting at 171 and 240 keV, both with a window of 20%. Images were reconstructed using 6 pixel-based ordered subset expectation maximization iterations with 16 subsets, a 0.2 mm isotropic voxel size and with decay and scatter corrections integrated into the unfiltered reconstruction [20]. Volume-rendered images were generated and analyzed using Amide Medical Image Data Examiner version 1.0.42 and MATLAB version 9.9.0.

Mice were scanned directly after their first injection and after 4, 24, 48, 72, and 96 h. Before every scan, mice were weighed and radioactivity in the total mouse was measured in a dose calibrator. Two IT-injected mice had very low total radioactive signal at the first measurement (0.3 and 0.1 MBq), indicating a failed injection, and were therefore excluded from the study (Supplementary Fig. S1).

Biodistribution studies

The mice were sacrificed 4 days after injection, directly after the last SPECT scan by cardiac exsanguination, and decapitated directly afterward. Tissues were excised for use in quantitative biodistribution studies. Tissues were weighed and counted for their radioactive content using a gamma counter (2470 automatic gamma counter; Perkin–Elmer). Counts per minute (CPM) were converted into decay-corrected MBq at the time point of injection ($t = 0$): disintegrations per minute (DPM). The biodistribution is expressed as the percentage of injected dose (%ID) and was calculated by dividing decay corrected CPM by DPM (CPM/DPM × 100). Efficiency was corrected for weight of the tissue (%ID/g) and this was corrected for the weight of the mouse to result in the standard uptake value. To calculate the amount of excreted radioactivity, the entire mouse was weighed and counted for radioactivity in a dose-calibrator.

At the time of dissection, and after the removal of the tissues, the radioactivity in the mice was recalculated. Excreted radioactivity (in urine and feces) was then calculated as (radioactivity of injected dose) − (radioactivity of excised tissues + radioactivity carcass). The following tissues were collected and stored in paraformaldehyde (PFA) for gamma counting: blood (cardiac), urine (urinary bladder), salivary gland, thyroid gland, lungs, heart, liver, gallbladder, kidneys, spleen, stomach, small intestines, large intestines, inguinal lymph nodes, muscle (paw), skin, fat (neck), bone, and pancreas.

The right hemisphere of the brain was fixed in PFA for gamma counting as well as immunohistochemical staining. The left hemisphere of the brain was dissected into the following areas: olfactory bulb, hippocampus, striatum, cortex, midbrain, cerebellum, brainstem, and spinal cord. For each brain area half was used for gamma counting and the other half was snap frozen in liquid nitrogen and stored at −80°C to be used for RNA analysis.

RNA analysis

Isolation of RNA from brain tissue was performed using TRIzol (15596026; Invitrogen) and the PureLink RNA Mini Kit (12183025; Thermo Fisher Scientific), as described before [21]. In short, ~100 mg of tissue was lysed with 1 mL TRIzol in MagNA Lyser tubes (3358941001; Roche) using a bullet blender (BBY24M; Next Advance) for 3 min on setting 8. After 5 min of incubation, 200 μL of chloroform was added and samples were centrifuged at 12,000*g* for 15 min. The aqueous phase was removed and added to an equal volume of 70% ethanol. Further RNA purification was performed using the PureLink RNA Mini Kit in accordance with the manufacturer's protocol and using a 15 min DNase step. RNA was eluted in 35 μL nuclease-free water.

Isolation of RNA from cultured cells was performed using the ReliaPrep RNA cell Miniprep System (Promega) according to manufacturer's instructions.

Synthesis of cDNA was performed with 500 ng of RNA using the Transcriptor First Strand cDNA Synthesis Kit (Roche), using random hexamer primers. The template-primer mixture was denatured for 10 min at 65°C. The cDNA synthesis reaction was performed for 10 min at 25°C and 30 min at 55°C and it was stopped for 5 min at 85°C, according to manufacturer's instructions.

Subsequently, polymerase chain reaction (PCR) was performed using primers in mouse APP exon 14 and 16

(Table 1). The PCR reaction was performed with 5 μL cDNA, FastStart Taq DNA Polymerase (Roche), 20 mM MgCl2, and 0.25 mM dNTPs. The PCR program started with denaturation at 95°C for 4 min, followed by 40 cycles of denaturation at 95°C for 10 s, annealing at 57°C for 30 s and elongation at 72°C for 20 s. The program was ended by a final elongation step at 72°C for 7 min and a cooling step at 4°C for 30 s. The PCR products were separated by electrophoresis on a 1.5% agarose gel containing 0.002% ethidium bromide.

Results

The addition of a DOTA chelator to the AON does not interfere with exon skipping

To label the AON with radioactive indium-111, a DOTA chelator is covalently bound to the AON using a linker (Fig. 1A). To determine if the AON conjugated to DOTA (AON-DOTA) can still bind to the target RNA and would still lead to exon skipping of exon 15 in APP, we transfected mouse neuroblastoma cells (N1E-115-1) with either AON or AON-DOTA in increasing concentrations. We showed with reverse transcriptase PCR (RT-PCR) that the conjugated AON could still bind to the target and RNA and exon skipping efficiencies were not affected by linking the DOTA label to the AON (Fig. 1B).

CNS retains higher levels of ^{111}In-AON activity over time compared to the rest of the body

Next, we labeled the AON-DOTA with radioactive indium-111 (AON-indium; Fig. 2A), and prepared 10 μL injections with 220 ± 21.2 μg AON and 31.1 ± 7.3 MBq of activity per injection ($n = 9$). Mice were injected with either an IT or an ICV injection. The mean whole-body activity directly after injection was 28.9 ± 7.7 MBq ($n = 4$) for the ICV-injected mice and 6.0 ± 3.4 MBq ($n = 5$) for the IT-injected mice. Directly after injection, mice were scanned in the SPECT scanner for 20 min. The scan was repeated at 4, 24, 48, 72, and 96 h after injection (Fig. 2B).

Total body radioactivity over time was measured in two ICV-injected and four IT injected mice. In the 96 h after the injections, there was a decrease of signal (Fig. 2C and Supplementary Fig. S2). The signal was corrected for decay and body weight, and is shown as a fraction of activity compared to T0. In the ICV-injected mice after 4 h, the signal had dropped to about 75%, and after this, steadily decreased over time to about 25% after 96 h (Fig. 2C). When comparing the total body reactivity to the SPECT, this drop in total body radioactivity was confirmed and showed that the signal was distributed throughout the body of the mice (Fig. 2D, E).

Furthermore, the signal after ICV injection was highest at the injection site, and started spreading through the CNS directly after injection (Fig. 2D). After 4 h, accumulation could be seen throughout the brain and spinal cord, as well as in the kidneys, the liver, and urine bladder. After 24 h, the signal in the brain decreased, and the signal in the kidneys increased. Over the course of the next days, the signal decreased rapidly in the kidneys, while it stayed at a relatively high level in the CNS. The signal is relatively stable in the liver, but when comparing signal intensities, the brain signal seems to be retaining more signal than the liver during the last

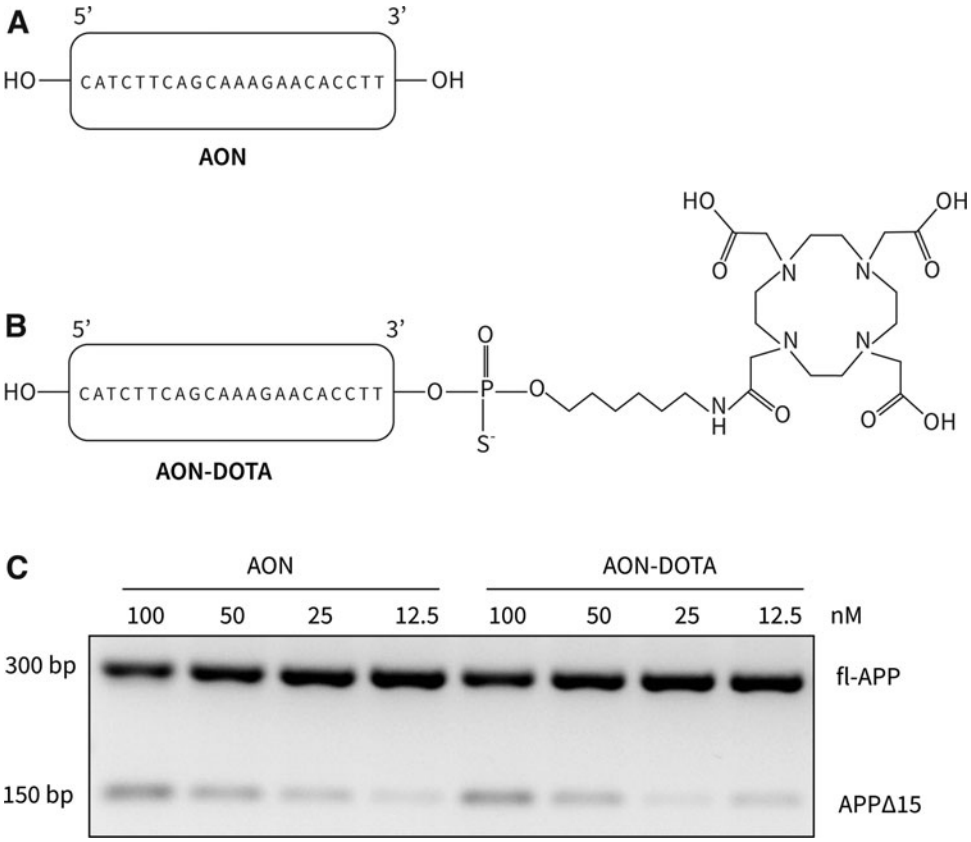

FIG. 1. Exon skipping efficiency was not affected by linking the DOTA label to the AON. **(A)** Schematic structure of the AON without chelator. **(B)** Structure of the AON with the linker and DOTA attached (AON-DOTA) (not to scale). **(C)** RT-PCR gel showing the AON-DOTA gives similar exon skip results as the AON without DOTA. The fl-APP can be seen at 299 bp and the skipped version of APP (APPΔ17) can be seen at 152 bp. Neuroblastoma cells (N1E-115-1) were transfected with 100, 50, 25, and 12.5 nM AON. AON, antisense oligonucleotide; fl-APP, full-length amyloid precursor protein; DOTA, 1,4,7,10-tetraazacyclododecane-1,4,7,10-tetraacetic acid; RT-PCR, reverse transcriptase PCR.

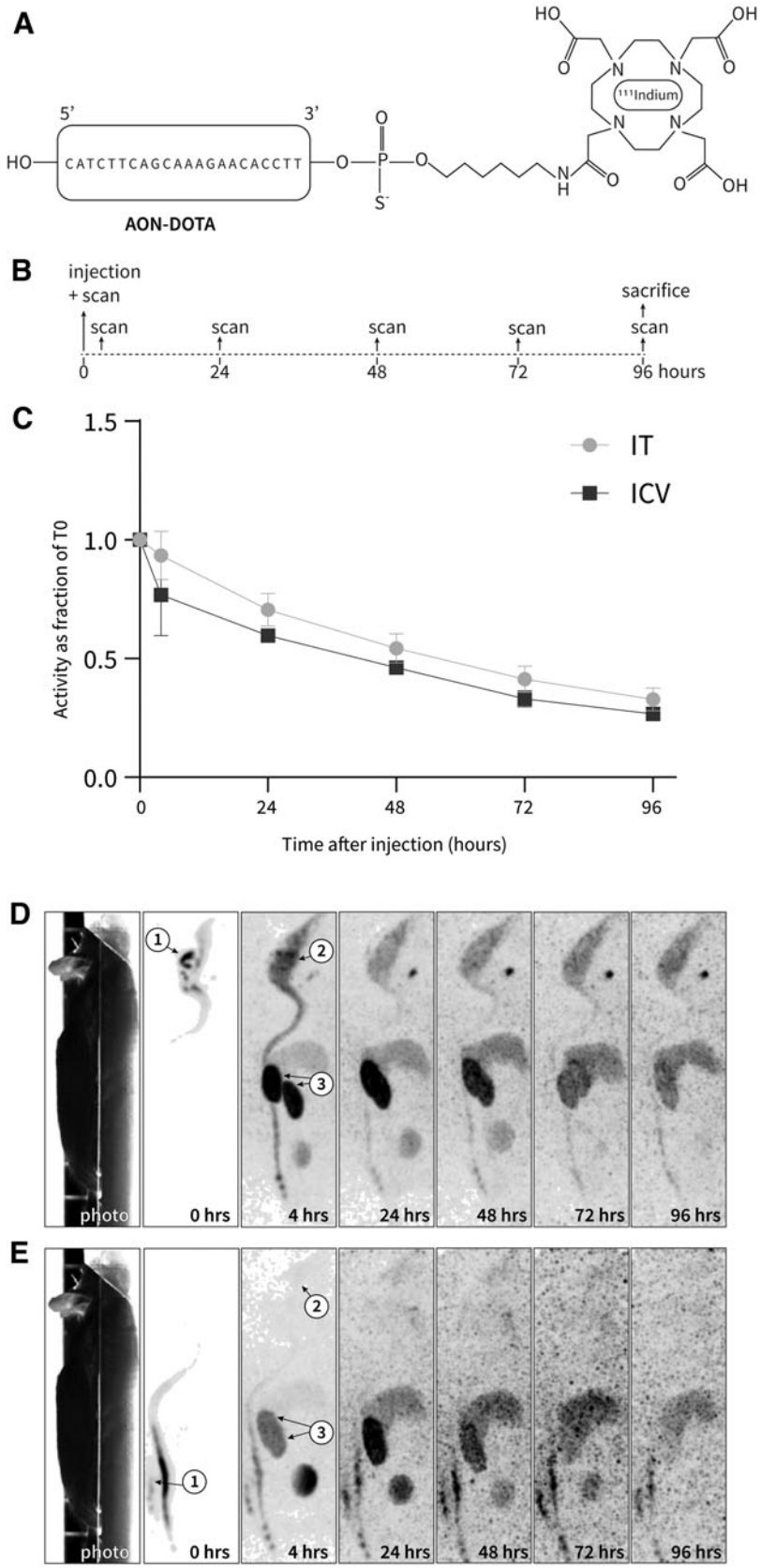

FIG. 2. Radioactive measurements of ICV- and IT ^{111}In-AON-injected mice over the course of 96 h were similar throughout the body with IT injection showing lower levels in the brain compared to ICV injection. **(A)** Schematic representation of AON labeled with indium-111. **(B)** Experimental timeline. **(C)** Before each SPECT scan, a whole-body measurement of ^{111}In-AON activity was performed; $n=2$ ICV injected and $n=4$ IT injected. This graph shows the ^{111}In-AON activity corrected for decay and weight, and as percentage of the first measurement. **(D, E)** Images of a representative scintigram of an ICV- **(D)** and IT **(E)**-injected mouse at the different time points, the first picture is a side view from the scanner. The images show cumulative ^{111}In-AON activity in the sagittal plane. Highlighted with *numbers* are the (1) injection site, (2) the brain, and (3) the kidneys. These representative images are taken from the total of four ICV-injected mice, and five IT-injected mice. ICV, intracerebroventricular; IT, intrathecal; SPECT, single-photon emission computed tomography.

three time points because the brain:liver ratio goes up (Supplementary Fig. S3). Some of the signal was detected in the thyroid gland, indicative of unattached ^{111}In [14].

In the IT-injected mice, a similar signal distribution over time was observed (Fig. 2E). The scintigram at T0 showed the spread of the ^{111}In-AON activity in the spinal cord directly after injection. After 4 h, the signal spread to the brain, but the levels were much lower than in the ICV-injected mice. Similar to the ICV-injected mice, the signal in the kidneys increased up to 24 h and decreased rapidly after this, while the brain showed low, but persistent retention.

^{111}In-AON activity is distributed in similar way in the mouse 96 h after ICV or IT injection

Mice were sacrificed after 96 h, and the dissected tissues were measured for ^{111}In-AON activity. ^{111}In-AON activity was the highest in the kidneys and liver (Fig. 3A) and distribution was similar across all tissues for both ICV- and IT-injected mice, suggesting that AON that is eliminated from CSF after IT or ICV administration distributes in a similar manner to systemic tissues. In the CNS, the signal was higher in ICV-injected mice compared to IT-injected mice but the

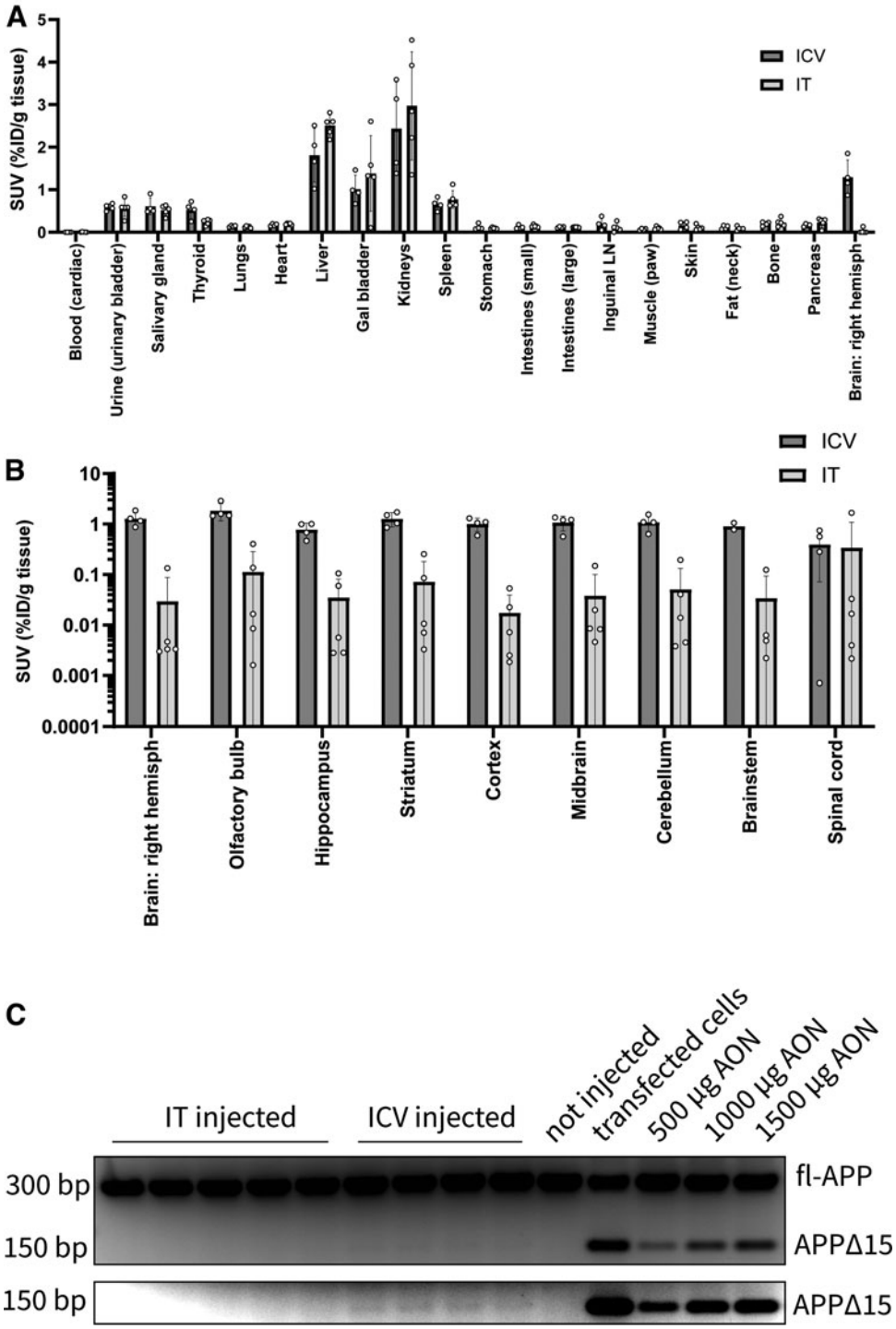

FIG. 3. Similar distribution of ^{111}In-AON activity in different tissues and brain regions, measured postmortem after ICV and IT injection. **(A)** ^{111}In-AON activity in peripheral tissues and in the brain (hemisphere) in ICV (*dark blue*) and IT (*light blue*)-injected mice. SUV are a radioactive counts per minute corrected for decay and body weight, and expressed as percentage of the ID per tissue mass. **(B)** ^{111}In-AON activity different brain regions in ICV- and IT-injected mice. The corrected counts are depicted on a $\log_{10}$-scale. **(C)** RT-PCR gel showing faint bands for the exon skipped product (APPΔ17) at 152 bp in ICV-injected mouse cortex, a digitally enhanced image below the blot shows the bands more clear. IT-injected mouse cortex did not show any band. Positive controls were from mouse neuroblastoma cells transfected with the same AON and from cortex of mice ICV treated with the same AON at higher doses (500, 1,000, and 1,500 µg). ID, injected dose; SUV, standard uptake values.

distribution of the signal was similar across all brain regions for both IT- and ICV-injected mice (Fig. 3B). This confirmed our imaging findings of the activity over time.

Interestingly, despite the much lower brain levels in the IT-injected mice, the spinal cord showed comparable ^{111}In-AON activity between ICV- and IT-injected mice. The standard deviation in the IT-injected mice was higher than in the ICV-injected mice. This can be explained by the technical difficulty of injecting in the mouse spinal canal.

Although this study was suboptimal for detecting a functional exon skipping effect because of the relatively low dose and short time after injection, there was a faint truncated PCR product on an overexposed image of a gel of an RT-PCR on mouse APP. This indicated low levels of splice modulating of APP mRNA in cortex tissue of ICV-injected mice only (Fig. 3C and Supplementary Fig. S4A, B).

Discussion

In the current study, we showed that the biodistribution and clearance of ^{111}In-labeled AONs is comparable for ICV and IT administration routes in mice. However, large differences in total delivered dose are found between IT and ICV injection. This difference in delivered dose could be explained by the partially missed IT injections, differences in signal intensity between IT- and ICV-injected mice along the spinal cord at 4 h postinjection confirm this explanation (data not shown). Immediately after injection, ^{111}In activity in the kidney was highest due to renal clearance of the AON. Over time, the AON was rapidly cleared systemically, while imaging and postmortem analysis showed robust retention of the AON in the brain.

In addition, signal intensity increases relatively in the brain compared to the liver during the last three time points. This indicates that AONs are not cleared from the brain as rapidly as from peripheral organs such as liver and kidney.

Although equal volumes were injected with ICV and IT, whole-body radioactivity levels showed that AON levels were much lower in IT-injected mice directly after injection. This can be explained by technical difficulties of injecting into the mouse spinal cord, which is small. In many cases, part of the dose was found in the needle or spilled. In two cases the procedure failed, and these mice were excluded from the study.

It is clear that technical difficulties will lead to higher variability in measurements, but IT injections also lead to relatively lower signal in the brain compared to ICV injections. A potential reason for this is that the IT injection site is further away from the brain than the ICV injection site. In addition, the circulation of CSF in the spinal cord is rostral to caudal, making it more difficult for AONs to reach the brain [12]. Despite lower intensity of ^{111}In-AON signal in the brain after IT injection compared to ICV, the levels and distribution of ^{111}In-AON activity over the peripheral organs measured postmortem is quite similar. There is, however, a higher ^{111}In-AON signal in the spinal cord of IT-injected mice and a lower signal in the brain regions analyzed.

Although overall levels were higher across brain regions in ICV-injected mice, the distribution throughout the brain was relatively even for both ICV- and IT-injected mice. Practically this would mean that when IT delivery is used in mouse studies, more frequent deliveries, or higher doses, would be needed to reach the same levels of AON throughout the brain than with ICV delivery. Alternatively, achieving higher brain concentrations after IT delivery might be achieved after continuous infusion with an injection pump [22]. However, for AON studies, it is known that bolus injections lead to more efficient treatment effects than continuous infusion delivery [8].

The distribution after IT injection of our splice-modulating AON over time was similar as was reported in a previous study for a gapmer AON-injected IT in rats, where it was shown that AONs rapidly spread throughout the CSF along the neuraxis, to the meninges, before entering the brain through penetrating arteries [12].

Our findings are in accordance with a simulated model of a splice modulating AON for spinal muscular atrophy, which showed initial high AON concentrations in plasma and CSF with the plasma and systemic tissue AON concentrations decreasing to much lower levels than the CSF and CNS tissue [23]. By adding a label to an AON, it is always possible that the label is detached from the AON or distribution is affected by the label. However, since our study is in agreement with previous distribution studies [12,23,24], with the exon skipping efficiencies in mouse brain from our previous study with an unlabeled AON [2,21], this suggests that the activity signal in the current study represents AON localization.

For clinical purposes, administration of AON to the human brain is being optimized continuously. Systemic delivery to the CNS is being developed with delivery aids, such as peptides [25], nanoparticles [26], exosomes [27], and receptor-mediated passage of the BBB [28], however, these delivery systems are not yet optimal and need high dosing to be effective. Ligand-conjugated AONs, as developed for liver delivery [29], could potentially offer systemic delivery to brain in the future. Intranasal delivery is an alternative option for delivery directly into the CNS [30], but mucus and metabolizing enzymes make it hard to get the AON in the CNS.

Injection into the lateral ventricle could be realized with a permanent cannula and an injection pump or Ommaya reservoir, which would make repeated dosing more safe and efficient. This ICV delivery has been used successfully in the treatment of conditions such as neurodegenerative diseases [31,32], intractable pain [33], and cancer [34]. However, this is quite an invasive procedure and infection [35] and complications related to the implant procedure [34] have been reported making IT delivery still the current preferred method of delivery for ASOs.

In preclinical research, IT injection would more closely resemble the current clinical practice. However, we showed that IT delivery in mice is challenging, because of the small size of the spinal canal. Importantly, IT and ICV injection in mice show comparable biodistribution over time. Furthermore, because similar doses lead to higher amounts of AON in the brain with ICV injection, higher effective dosing can be accomplished than with IT, and therefore ICV may remain the preferred AON delivery method for most preclinical applications.

Author Disclosure Statement

D.C., PhD, T.T.H., and T.d.V. have been under the employment of Amylon Therapeutics B.V. or its subsidiary Amylon Therapeutics, Inc., and all own stock in the company. The other authors declare no conflicts of interest. T.M. and W.M.C.v.R.M. are members of the European COST Action DARTER (CA17103).

Funding Information

This research was funded by ZonMw Memorabel [733050818], under the project name: RNA modulation therapy for Alzheimer's disease.

Supplementary Material

Supplementary Figure S1
Supplementary Figure S2
Supplementary Figure S3
Supplementary Figure S4

References

1. Wurster CD, B Winter, K Wollinsky, AC Ludolph, Z Uzelac, S Witzel, M Schocke, R Schneider and T Kocak. (2019). Intrathecal administration of nusinersen in adolescent and adult SMA type 2 and 3 patients. J Neurol 266: 183–194.
2. Daoutsali E, TT Hailu, RaM Buijsen, BA Pepers, LM Van Der Graaf, MM Verbeek, D Curtis, T De Vlaam and WMC Van Roon-Mom. (2021). Antisense oligonucleotide-induced amyloid precursor protein splicing modulation as a therapeutic approach for dutch-type cerebral amyloid angiopathy. Nucleic Acid Ther 31:351–363.
3. Jauvin D, J Chrétien, SK Pandey, L Martineau, L Revillod, G Bassez, A Lachon, AR Macleod, G Gourdon, *et al.* (2017). Targeting dmpk with antisense oligonucleotide improves muscle strength in myotonic dystrophy type 1 mice. Mol Ther Nucleic Acids 7:465–474.
4. Finkel RS, E Mercuri, BT Darras, AM Connolly, NL Kuntz, J Kirschner, CA Chiriboga, K Saito, L Servais, *et al.* (2017). Nusinersen versus sham control in infantile-onset spinal muscular atrophy. N Engl J Med 377:1723–1732.
5. Monine M, D Norris, Y Wang and I Nestorov. (2021). A physiologically-based pharmacokinetic model to describe antisense oligonucleotide distribution after intrathecal administration. J Pharmacokinet Pharmacodyn 48: 639–654.
6. Hua Y, K Sahashi, G Hung, F Rigo, MA Passini, CF Bennett and AR Krainer. (2010). Antisense correction of smn2 splicing in the CNS rescues necrosis in a type III SMA mouse model. Genes Dev 24:1634–1644.
7. Kordasiewicz Holly B, LM Stanek, EV Wancewicz, C Mazur, MM Mcalonis, KA Pytel, JW Artates, A Weiss, SH Cheng, *et al.* (2012). Sustained therapeutic reversal of Huntington's disease by transient repression of Huntingtin synthesis. Neuron 74:1031–1044.
8. Rigo F, SJ Chun, DA Norris, G Hung, S Lee, J Matson, RA Fey, H Gaus, Y Hua, *et al.* (2014). Pharmacology of a central nervous system delivered 2′-o-methoxyethyl-modified survival of motor neuron splicing oligonucleotide in mice and nonhuman primates. J Pharmacol Exp Ther 350:46–55.
9. Ramos DM, C D'ydewalle, V Gabbeta, A Dakka, SK Klein, DA Norris, J Matson, SJ Taylor, PG Zaworski, *et al.* (2019). Age-dependent smn expression in disease-relevant tissue and implications for sma treatment. J Clin Invest 129: 4817–4831.
10. Sullivan JM, C Mazur, DA Wolf, L Horky, N Currier, B Fitzsimmons, J Hesterman, R Pauplis, S Haller, *et al.* (2020). Convective forces increase rostral delivery of intrathecal radiotracers and antisense oligonucleotides in the cynomolgus monkey nervous system. J Transl Med 18:309.
11. Khani M, BJ Lawrence, LR Sass, CP Gibbs, JJ Pluid, JN Oshinski, GR Stewart, JR Zeller and BA Martin. (2019). Characterization of intrathecal cerebrospinal fluid geometry and dynamics in cynomolgus monkeys (*Macaca fascicularis*) by magnetic resonance imaging. PLoS One 14: e0212239.
12. Mazur C, B Powers, K Zasadny, JM Sullivan, H Dimant, F Kamme, J Hesterman, J Matson, M Oestergaard, *et al.* (2019). Brain pharmacology of intrathecal antisense oligonucleotides revealed through multimodal imaging. JCI Insight 4:e129240.
13. Toonen LJA, J Casaca-Carreira, M Pellise-Tintore, H Mei, Y Temel, A Jahanshahi and WMC Van Roon-Mom. (2018). Intracerebroventricular administration of a 2′-o-methyl phosphorothioate antisense oligonucleotide results in activation of the innate immune system in mouse brain. Nucleic Acid Ther 28:63–73.
14. Welling MM, SJ Spa, DM Van Willigen, DDD Rietbergen, M Roestenberg, T Buckle and FWB Van Leeuwen. (2019). In vivo stability of supramolecular host–guest complexes monitored by dual-isotope multiplexing in a pre-targeting model of experimental liver radioembolization. J Control Release 293:126–134.
15. Aartsma-Rus A. (2012). Overview on aon design. Methods Mol Biol 867:117–129.
16. Van De Steeg E, T Läppchen, B Aguilera, HT Jansen, D Muilwijk, R Vermue, JW Van Der Hoorn, K Donato, R Rossin, *et al.* (2017). Feasibility of spect-ct imaging to study the pharmacokinetics of antisense oligonucleotides in a mouse model of duchenne muscular dystrophy. Nucleic Acid Ther 27:221–231.
17. Fairbanks CA. (2003). Spinal delivery of analgesics in experimental models of pain and analgesia. Adv Drug Deliv Rev 55:1007–1041.
18. Metz T, EC Kuijper and WMC Van Roon-Mom. (2022). Delivery of antisense oligonucleotides to the mouse brain by intracerebroventricular injections. Methods Mol Biol 2434:333–341.
19. Welling MM, N Duszenko, DM Van Willigen, WK Smits, T Buckle, M Roestenberg and FWB Van Leeuwen. (2021). Cyclodextrin/adamantane-mediated targeting of inoculated bacteria in mice. Bioconjug Chem 32:607–614.
20. Welling MM, N Duszenko, DM Van Willigen, AW Hensbergen, T Buckle, DDD Rietbergen, M Roestenberg and FWB Van Leeuwen. (2021). Interventional nuclear medicine: ''Click'' chemistry as an in vivo targeting strategy for imaging microspheres and bacteria. Biomater Sci 9:1683–1690.
21. Toonen LJA, F Rigo, H Van Attikum and WMC Van Roon-Mom. (2017). Antisense oligonucleotide-mediated removal of the polyglutamine repeat in spinocerebellar ataxia type 3 mice. Mol Ther Nucleic Acids 8:232–242.
22. Wang D, J Li, K Tran, DR Burt, L Zhong and G Gao. (2018). Slow infusion of recombinant adeno-associated viruses into the mouse cerebrospinal fluid space. Hum Gene Ther Methods 29:75–85.
23. Luu KT, DA Norris, R Gunawan, S Henry, R Geary and Y Wang. (2017). Population pharmacokinetics of nusinersen in the cerebral spinal fluid and plasma of pediatric patients with spinal muscular atrophy following intrathecal administrations. J Clin Pharmacol 57:1031–1041.
24. Jafar-Nejad P, B Powers, A Soriano, H Zhao, DA Norris, J Matson, B Debrosse-Serra, J Watson, P Narayanan, *et al.* (2020). The atlas of RNAse H antisense oligonucleotide

distribution and activity in the CNS of rodents and non-human primates following central administration. Nucleic Acids Res 49:657–673.
25. Hammond SM, G Hazell, F Shabanpoor, AF Saleh, M Bowerman, JN Sleigh, KE Meijboom, H Zhou, F Muntoni, *et al.* (2016). Systemic peptide-mediated oligonucleotide therapy improves long-term survival in spinal muscular atrophy. Proc Natl Acad Sci U S A 113:10962–10967.
26. Male D and R Gromnicova. (2022). Nanocarriers for delivery of oligonucleotides to the CNS. Int J Mol Sci 23:760.
27. Alvarez-Erviti L, Y Seow, H Yin, C Betts, S Lakhal and MJA Wood. (2011). Delivery of siRNA to the mouse brain by systemic injection of targeted exosomes. Nat Biotechnol 29:341–345.
28. Kozlu S, S Caban, F Yerlikaya, E Fernandez-Megia, R Novoa-Carballal, R Riguera, M Yemisci, Y Gursoy-Ozdemir, T Dalkara, *et al.* (2014). An aquaporin 4 antisense oligonucleotide loaded, brain targeted nanoparticulate system design. Pharmazie 69:340–345.
29. Prakash TP, J Yu, MT Migawa, GA Kinberger, WB Wan, ME Østergaard, RL Carty, G Vasquez, A Low, *et al.* (2016). Comprehensive structure-activity relationship of triantennary n-acetylgalactosamine conjugated antisense oligonucleotides for targeted delivery to hepatocytes. J Med Chem 59:2718–2733.
30. Shah P, M Lalan and K Barve. (2022). Intranasal delivery: An attractive route for the administration of nucleic acid based therapeutics for CNS disorders. Front Pharmacol 13: 974666.
31. Duma C, O Kopyov, A Kopyov, M Berman, E Lander, M Elam, M Arata, D Weiland, R Cannell, *et al.* (2019). Human intracerebroventricular (ICV) injection of autologous, non-engineered, adipose-derived stromal vascular fraction (ADSVF) for neurodegenerative disorders: Results of a 3-year phase 1 study of 113 injections in 31 patients. Mol Biol Rep 46:5257–5272.
32. Nutt JG, KJ Burchiel, CL Comella, J Jankovic, AE Lang, ER Laws, Jr., AM Lozano, RD Penn, RK Simpson, Jr., *et al.* (2003). Randomized, double-blind trial of glial cell line-derived neurotrophic factor (GDNF) in PD. Neurology 60:69–73.
33. Raffa RB and JV Pergolizzi, Jr. (2012). Intracerebroventricular opioids for intractable pain. Br J Clin Pharmacol 74:34–41.
34. Anton S, M Margold, T Kowalski, D Miller, K Schmieder, U Schlegel and S Seidel. (2021). Complications of intracerebroventricular chemotherapy via subgaleal reservoir in primary central nervous system lymphoma: A single-institution experience on 1247 installations in 94 consecutive patients. Hematol Oncol 39:176–184.
35. Szvalb AD, Raad, Ii, JS Weinberg, D Suki, R Mayer and GM Viola. (2014). Ommaya reservoir-related infections: Clinical manifestations and treatment outcomes. J Infect 68:216–224.

Address correspondence to:
Tom Metz, MSc
Department of Human Genetics
Leiden University Medical Center
Einthovenweg 20
Leiden 2300 RC
The Netherlands

E-mail: t.metz@lumc.nl

Received for publication April 3, 2023; accepted after revision August 30, 2023.